4-channel Differential Lock-In Amplifiers with Autobalancing Network for Stimulated Raman Spectroscopy

G. Sciortino, A. Ragni, A. De la Cadena, M. Sampietro, *Member, IEEE*, G. Cerullo, D. Polli, G. Ferrari, *Member, IEEE*

Abstract—We introduce a multi-channel integrated circuit for fast Stimulated Raman Scattering (SRS) microscopy on multiple simultaneous frequencies at a frame rate higher than 1 frame/s. The chip is a 4-channel differential readout system, based on the lock-in technique. It is able to measure down to 10 ppm SRS signal, over a wide range of input optical powers ($50\,\mu$W - $600\,\mu$W per channel), with a pixel dwell time of only $30\,\mu$s. Each acquisition channel includes 2 low-noise preamplifiers, 2 variable-gain amplifiers, a fully differential voltage subtractor and a lock-in demodulator. The differential readout electronics rejects the power fluctuations of the laser and it is automatically balanced by an analog feedback loop over $\pm\,30\,\%$ input power mismatches. Thanks to the autobalancing network, the pixel dwell time is reduced by a factor up to 225 with a settling time of only $10\,\mu$s. The chip is fabricated in AMS $0.35\,\mu$m CMOS technology and it is included in a combined electronics and optical system. Both single-pixel spectral measurements and multi-spectral imaging measurements are presented to validate the full SRS microscope.

Index Terms—Multichannel, Raman Spectroscopy, lock-in amplifier, differential, autobalancing, variable gain amplifier, peak detector, transimpedance, amplifier, noise cancelling

I. INTRODUCTION

Stimulated Raman Scattering (SRS) spectroscopy [1] [2] is a powerful third-order nonlinear optics technique, allowing one to generate and detect a vibrational coherence in a sample, thus measuring its vibrational spectrum. Combining SRS and microscopy, it is possible to obtain Raman images of samples with sub-micrometer spatial resolution. The technique allows a label-free, non-invasive and spatially resolved chemical identification of the sample [3], with important applications in chemistry [4], biology [5] [6] and cancer diagnosis [7] [8].

SRS-based microscopes excite the Sample Under Test (SUT) with two pulsed laser beams with different frequencies: the pump at ω_p and the Stokes at ω_S. If the Raman shift $\Delta\omega$ = ω_p - ω_S matches a vibrational mode Ω of the molecule observed, there is a finite probability that some pump photons are scattered to the Stokes frequency ω_S. The Stokes beam intensity I_S then experiences a gain (Stimulated Raman Gain - SRG = $\Delta I_S/I_S$) and correspondingly the Pump intensisty I_p experiences a loss (Stimulated Raman Loss - SRL = $\Delta I_p/I_p$) [1]. SRG and SRL spectra are proportional to the spontaneous Raman spectrum and thus provide a vibrational fingerprint of the excited molecules. Under typical operating conditions, SRG and SRL signals are of the order of $10^{-5} - 10^{-3}$ [9]. To distinguish such small signals from the fluctuating pump/Stokes background, a modulation transfer scheme is adopted, in which the Stokes(pump) beam is amplitude modulated at a high frequency f_m and the pump(Stokes) beam is synchronously demodulated, allowing the extraction of the SRL(SRG) signal. Modulation transfer enables to suppress low-frequency laser fluctuations and to achieve close to shot-noise-limited performance. The ΔI_p (ΔI_s) signal is indeed accordingly modulated at the same f_m, where it can be extracted from the mean power using the lock-in technique.

The growing demand for SRS microscopes with a fast frame rate ($>$ 1 frame/s) and sub-micrometer spatial resolution as required for biological applications [10] [11], calls for the development of an experimental setup with a careful minimization of the noise in order to have a short pixel dwell time. Commercial laser systems suitable for SRS have a noise limited by the random fluctuation of the optical power [12] [13] [14]. Although this so-called intensity noise is highly dependent on the laser model, it is a low-frequency noise that can be tens of times higher than the shot noise given by the Poisson statistics of the photon generation. To overcome this limit, a differential or balanced detection approach can be used, in which the probe laser beam (Stokes or Pump depending on SRG or SRL detection) is split in two replicas before the SUT. The first one, called Signal beam, passes through the sample, where it experiences the SRS effect. The second one is kept as Reference beam and it is directly focused on a second photodetector. Measuring the difference between the intensities of the two beams, the intensity noise of the laser is rejected as a common mode signal. The differential approach requires a careful balancing of the Signal and Reference incident powers in order to effectively cancel the common-mode noise and recover a shot-noise limited condition. A simple equalization of the Reference beam at the beginning of the experiment is not effective, because the attenuation of the beam passing through the sample varies from pixel to pixel. Thus, an active system is necessary, that continuously equalizes the Signal and Reference amplitudes to maximize the common mode noise rejection.

Standard SRS systems work at a single vibrational frequency Ω with very high image acquisition speeds up to the video rate. However, many applications require the measurement of the full SRS spectrum [15], in order to exploit its biochemical information. Many broadband SRS microscopes [16] [17] [14] [18] [19] follow a so called hyperspectral measuring approach which consists in sequentially scanning the
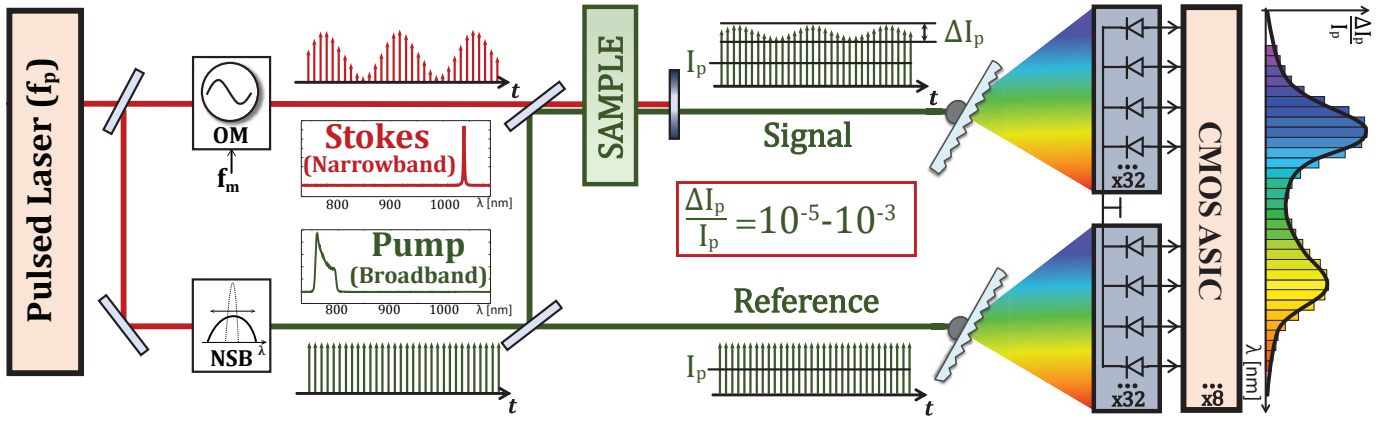
Fig. 1. Simplified scheme for the multiplex SRS microscope based on the detection of the SRL of the pump beam. NSB: non-linear spectral broadening component (an Optical Parametric Oscillator in our implementation); OM: optical modulator.

pump-Stokes frequency detuning, thereby acquiring an SRS spectrum, for every pixel of the image. While this method is effective under optimized conditions [20], even more appealing is multiplex SRS [21] [22] [23]. This approach, as shown in the simplified setup in Fig. 1, combines a broadband pump (Stokes) pulse with a narrowband Stokes (pump) pulse in order to probe in parallel many vibrational modes Ω, allowing to parallelize the SRS spectrum acquisition. The broadband pump (Stokes) beam, with the superimposed SRS signal, is spatially divided into different spectral components by means of a grating or a prism, focused onto a linear photodetector array and simultaneously acquired by a multichannel system. Thus, the multiplex solution allows a SRS spectrum acquisition with a single measurement for each pixel of the image.

The multichannel acquisition system is typically implemented with many lock-in amplifiers operated in parallel. Although lock-in amplifiers working up to MHz range with a fast response time ($\approx 10\,\mu s$) are commercially available, multiplex acquisition systems fully based on commercial instrumentation are bulky, expensive and currently limited to few kHz [22]. Tuned amplifiers have been proposed as an alternative to lock-in instruments [21]. The solution employs a custom discrete component electronic system with several tuned LC filters for the frequency selection of the SRS signals and uses peak detectors for the extraction of its amplitude. The drawbacks of this solution are the fixed by design SRS modulation frequency, the request for a careful calibration of the filters and the sub-optimal noise rejection operated by a peak detector with respect to the lock-in technique. A different architecture for a parallel acquisition is reported in [24] [25], where a 10x10 pixels CMOS lock-in camera with on-chip photodetectors is proposed. Although the frequency scanning is sequential, the frame rate is increased by the acquisition of several pixels in parallel in the space domain. However, the small area per pixel available sets severe limitations on the minimum achievable noise and consequently on the frame rate ($\ll$ 1 frame/s).

In this paper, we present the first multichannel CMOS readout circuit specifically designed for broadband SRS microscopy. The ASIC implements a low-noise lock-in detection

of the SRS signal simultaneously on four wavelengths. Differently from others lock-in-based integrated sensor interfaces (see [26] for a recent review), it has a differential current readout with an automatic balancing of the Signal and Reference paths. The compactness of an integrated solution and the performance reached by combining differential approach and the multichannel detection allow the development of a fast and sensitive SRS microscope for biological applications.

This paper is organized as follows. Section II provides an overview of the SRS microscope and the main specifications of the readout electronics. Section III details the implementation of the CMOS chip and section IV reports its electrical characterization. The experimental validation of a prototype of SRS microscope, based on the fabricated chip, is briefly reported in section V. Finally, section VI summarizes the achieved results.

II. SRS MICROSCOPE SYSTEM AND ASIC SPECIFICATIONS

Fig. 1 shows the simplified scheme of the broadband SRS microscope setup for which the chip has been designed. The optical source is a commercial laser that generates a pulsed light beam with repetition rate f_p. The beam is split in two replicas. The first one passes through a Non-linear Spectral Broadening element (NSB), that produces a broadband pump beam. The second one is called Stokes and, through an Optical Modulator (OM), is modulated in amplitude at f_m.

The pump beam is divided in two paths called Signal and Reference, respectively. The Signal pump replica and the Stokes beam are collimated and focused on the SUT. By passing through the sample, the pump experiences a SRL modulated at the same frequency f_m, as the Stokes. After the sample the Stokes is optically filtered and Signal and Reference pump are spatially dispersed by two diffraction gratings. The separated wavelengths are focused on two linear photodetector arrays directly connected to the ASICs. Our final microscope will process in parallel 32 wavelengths using eight 4-channel ASICs identical to the one presented in this paper. Each channel measures the modulated signal and the mean incident power to calculate the normalized SRS signal ($\Delta I_p / I_p$). The sensor chosen is the commercial photodiode

linear array A5C-35 by OSI Optoelectronics. The ASIC is designed to be compatible with different optical setups and laser sources. It is able to operate with a modulation frequency in the range of $1\,$MHz-$10\,$MHz and a repetition rate f_p between $20\,$MHz and $80\,$MHz with the best performance at $40\,$MHz. In the latter operating condition, the chip is able to manage a mean input power from $50\,\mu$W to $600\,\mu$W on each photodiode. Given an average photodiode's resposivity of 0.5 A/W, the generated current of each photodetector is a train of pulses with a mean value $\overline{I_{in}}$ between $25\,\mu$A and $300\,\mu$A respectively. In the ideal case of a shot-noise limited measurement, i.e. a negligible electronic noise and a cancellation of the laser intensity noise by a well-balanced differential readout, the minimum detectable normalized SRS signal is :

$$SRS_{min} = \frac{\sqrt{2q\overline{I_{in}}BW}}{\overline{I_{in}}} \tag{1}$$

where the numerator is the shot noise integrated on the lock-in bandwidth assuming a square wave modulation of the optical signal. By considering a minimum SRS signal SRS_{min} of 10 ppm, an optical input power of $100\,\mu$W and the photodiode's resposivity of 0.5 A/W, the maximum lock-in bandwidth is $\approx 16\,$kHz. The ASIC is designed to guarantee such acquisition speed by keeping the electronic noise power spectral density smaller than the shot noise level in the range of $50\,\mu$W-$600\,\mu$W input optical power. In addition, an auto-balancing network with an error lower than $1\,\%$ and a bandwidth greater than $16\,$kHz is required to cancel the effect of the laser intensity noise during the fast acquisition of an image. Finally, the ASIC should be compatible with a multichannel detection scheme, in particular down-converting the modulated SRS signal to low frequency for a simpler off-chip data acquisition.

III. ASIC ARCHITECTURE

Fig. 2 shows the architecture of the four-channel ASIC. Each channel presents a pre-amplification stage for the readout of the pulsed current, coming from the photodiode. The DC components of the input signal are available as outputs of the chip ($V_{o_{DC}}$) for the normalization of the SRS spectrum. The AC components instead pass through the Variable Gain Amplifers (VGAs). The gain of the VGA in the Reference path is tuned by an on-chip Automatic Gain Control network (AGC) in order to equalize the amplitudes of the Reference and Signal pulses, measured by two peak detectors. The fluctuations of the laser power are a common mode noise at the output of the VGAs, that is reduced by an analog fully differential AC coupled subtractor. The effectiveness of this differential approach was validated by a discrete-component prototype with a manual equalization of the amplitudes [27]. Finally, a coherent demodulator down-converts the SRS signal to low frequency, for a simpler data acquisition.

A. Preamplifer

The pulsed current coming from the photodiode is converted into a voltage by the charge preamplifier shown in Fig. 3. An active network made by the operational amplifier OA2, configured as a non-inverting integrator, drives the resistance R_{dc}

in order to force a zero mean value at the output $V_{out,pre}$ of the charge preamplifier [28] [29]. The output of OA2, $V_{o,DC}$, is directly proportional to the mean optical power incident on the photodetector. The low gain at high frequency of the active network leaves the fast current pulse to be integrated on the feedback capacitor C_f of the charge preamplifier. The closed loop transfer function of the preamplifier is:

$$G_{ac} = \frac{V_{out,pre}}{i_{in}} \approx -\frac{(sC_1 R_1)k R_{dc}}{(1 + sk R_{dc} C_f)(1 + sC_1 R_1)} \tag{2}$$

with $k = (R_a + R_b)/R_b$. The pole $R_1 C_1$ given by the non-inverting integrator is set at $80\,$kHz, well below the modulation frequency of the SRS signal ($1 - 10$MHz). C_f and R_{dc} are chosen to maximize the AC and DC gain for a given input power. The factor k is a free design parameter that can be tuned to obtain the desired frequency response at the SRS modulation frequency. We have implemented a fixed value of $k = 35$, so that the preamplifier transfer function behaves like an integrator starting from $500\,$kHz, with the gain G_{ac} fixed by C_f.

The input-referred current noise spectral density can be approximated as:

$$S_i \approx \frac{4kT}{R_1}\left(\frac{1}{\omega C_1 R_1}\right)^2 + \frac{4kT}{R_{dc}} + \overline{e_1^2}\omega^2\left(C_{in} + C_f\right)^2 \tag{3}$$

where $\overline{e_1^2}$ is the input-referred voltage noise of OA1 and $C_{in} \approx 15$pF is the total capacitance at the input node, dominated by the photodetector capacitance ($10\,$pF). R_{dc} and C_f should be maximized and minimized, respectively, to obtain the electronic noise below the shot noise of the photodiode. Four couples of C_f and R_{dc} are selectable using two digital bits in order to optimize the values depending on the input optical power, as shown in Fig. 3. A voltage noise of OA1 as low as $\overline{e_1^2} = 2.4\,$nV$/\sqrt{\text{Hz}}$ is obtained with the scheme reported in Fig. 4. It is a low noise Miller compensated folded amplifier, with near rail-to-rail output stage [30]. Two resistances $R_s = 20\,\Omega$ are inserted at the source terminal of the input transistors in order to decrease the closed-loop bandwidth, without reducing the first stage bias current, i.e. increasing the noise. This allows a linear behaviour in response to the input current pulse, without limitations given by the internal slew rate. The bandwidth of the closed loop amplifier depends on the C_f selected and ranges between $100\,$MHz to $200\,$MHz.

B. Variable Gain Amplifier

The expected relative amplitude mismatch between Reference and Signal pulses is $\pm 30\,\%$, mainly given by the local variability of the optical absorption/scattering of the sample. The amplitudes of the pulses are equalized using the VGA shown in Fig. 5. The core of the circuit is a differential stage (M_1 and M_2) with the transconductance $g_{m,1-2}$, i.e. the gain, controlled by the voltage V_{var} through the tail current source M_6. The differential current of M_1 and M_2 is converted into a
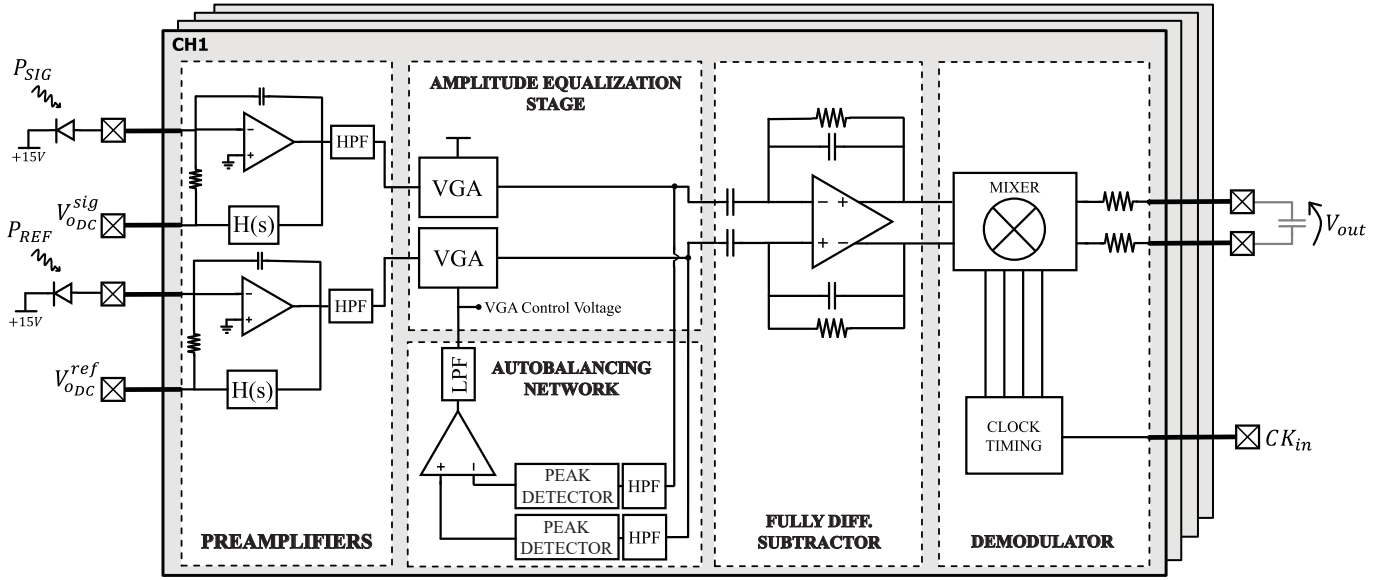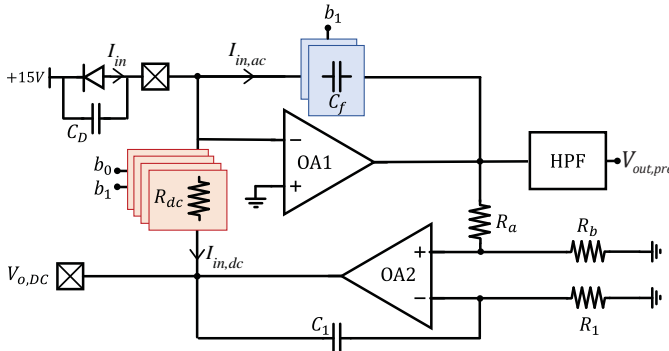
Fig. 2. Architecture of a single channel with the main functional blocks: the low noise preamplifier, that amplifies and separates the DC and AC components, the amplitude equalization stage with the autobalancing network, the fully differential subtractor and the demodulator.

b1,b0	C_f[pF]	R_{dc}[kΩ]	$I_{in,dc}^{max}$ [μA]	$(P_{in,max}$[μW])	Other design parameters	
00	1.15	20	50	100	R_a [kΩ]	34
01	1.15	10	100	200	R_b [kΩ]	1
10	2.3	5	200	400	R_1 [kΩ]	1000
11	2.3	3.6	300	600	C_1 [pF]	2

Fig. 3. Schematic of the preamplifier. The AC signal is amplified by the selectable capacitance C_f, while the DC component is drained by the OA2 opamp and, passing through the selectable resistance R_{dc}, is measured at the output PAD $V_{o,DC}$. The values of C_f and R_{dc} selected by the digital bit B0 and B1 are shown in the table.
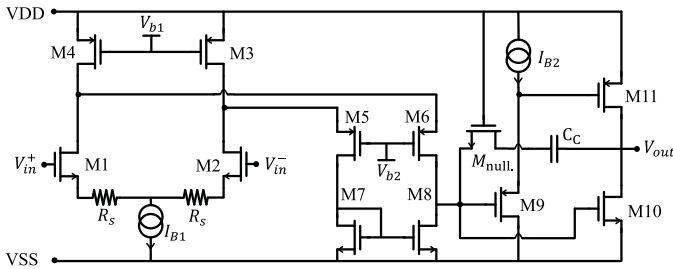

Fig. 4. Schematic of the low noise amplifier OA1.

voltage using the resistive load R_3 and R_4 giving a single-end small-signal gain approximately of
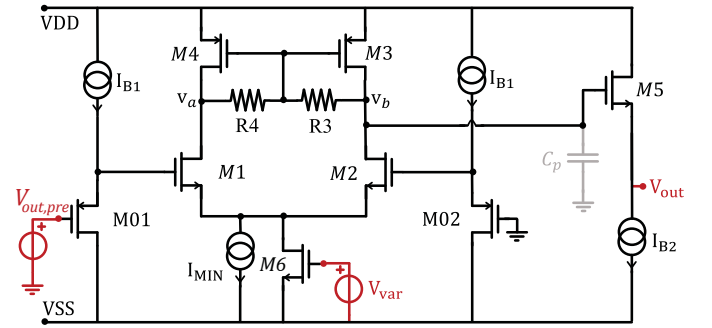

Fig. 5. Schematic of the Variable Gain Amplifier.

$$G_{VGA} \approx \frac{g_{m,1-2}}{2} \left(r_{o3}//R_3 \right) G_{foll_{in}} G_{foll_{out}} \qquad (4)$$

where $G_{foll_{in}}$ and $G_{foll_{out}}$ are the gains of the input and output follower stages (made by M_{01} and M_5 respectively) and r_{o3} is the output resistance of M_3. We set R_3 to $11\,\mathrm{k\Omega}$ to obtain a nominal gain adjustable between 0.6 and 1.2 through V_{var}. The VGA on the Signal path has a gain fixed to 0.9 allowing a compensation range of $\pm 33\%$ on the Reference path. The variation of the output bias voltage given by a change of the gain is reduced by connecting R_3 and R_4 to the gates of M_3 and M_4. The tail current controlled by V_{var} cannot flow through R_3 and R_4 forcing a trans-diode configuration of M_3 and M_4 on the common-mode. Thus, a sub-linear response of the v_a and v_b bias voltage is obtained. In addition to the equalization of the Signal and Reference amplitudes, an effective subtraction in the time domain requires well-matched phases and non-linearity errors on the two paths. We reduced the mismatch between the phases by keeping the bandwidth of the VGA well above the pulse frequency f_{pulse} of $40\,\mathrm{MHz}$. The simple VGA architecture and the output follower, that reduces the parasitic capacitance at the gain node v_b, allow a

bandwidth greater than $300\,\text{MHz}$ in all gain conditions. The non-linearity error of the VGA is limited by the differential couple $M_1 - M_2$. It is reduced by increasing the overdrive voltage of the two transistors up to $1.1\,\text{V}$ with the maximum bias current. The input follower stages (M_{01} and M_{02}) shift the input DC bias point of the differential stage in order to keep the tail generators (I_{MIN} and M_6) in saturation regime. Moreover, the resistor R_4 is lower than R_3 ($R_4 = R_3/6$) in order to limit the voltage differential swing of the node v_a, avoiding an operation in triode region of M_1.

C. Automatic Gain Control network

An effective differential suppression of the excess intensity noise of the laser, which can be up to tens of times higher than the shot noise, requires an equalization of the Signal and Reference amplitudes accurate to a few percents. Unlike previous implementations of CMOS differential lock-in amplifiers where the balancing of the differential structure is done off-chip [31]–[33] or slowly just to avoid the saturation of the amplifiers [34], in imaging applications the balancing must be automatic and fast in order to compensate the Reference and Signal amplitudes for each pixel. A discrete component board with an automatic balancing network based on an analog multiplier and a variable phase shifter has been reported in [13]. The complexity of the feedback loop limits the response time to $\approx 15\,\text{ms}$, not suitable for a fast pixel dwell time acquisition. A faster solution is proposed in [14] in which the DC harmonics are used to estimate the amplitude mismatches. It requires four commercial VGAs per channel and the accuracy is limited by the mismatches between the VGAs. In [9] [35] the problem is partially solved with a fully optical approach, which however increases the optical power on the SUT and it requires a careful calibration before each measurement.

In this work a fine tuned equalization is obtained with an on-chip network that automatically measures the power differences between the two input beams and varies the gain of the Reference acquisition channel accordingly. This autobalancing network has a fast settling time of $10\,\mu\text{s}$, does not require additional power on the SUT neither an external calibration. Moreover, the circuital simplicity of the solution has allowed the integration of an independent AGC for each channel.

The main frequency components of the input train of pulses available to estimate the relative amplitude mismatches are the $0\,\text{Hz}$ and the f_{pulse} harmonics. Since the DC spectral component has been filtered after the preamplifier stage, the feedback loop designed for the automatic equalization (Fig. 6a) measures the AC signal amplitude using a peak detector for each channel. The integral of the amplitude difference is used to control the gain of the VGA on the Reference path. The VGA along the Signal path has a constant gain in order to have a fixed amplification of the SRS signal. This VGA is only added to match the frequency response of the two paths. The scheme of the peak detector is shown in Fig. 6b. We have modified the architecture in [36] for a free-running operation without a digital reset. When the input voltage $V_{peak,in}$ is greater than $V_{peak,out}$, the transistor M5 is turned on and the capacitor $C = 500\,\text{fF}$ is

charged by M6. The buffer configuration of the circuit ensures $V_{peak,out} \approx V_{peak,in}$. When the input voltage becomes smaller than the output, the transistors M5-M6 are switched off, C maintains the charge and the output voltage $V_{peak,out}$ holds the maximum value reached by the input voltage. The current source $I_{leak} = 500\,\text{nA}$ slowly discharges C in order to track the amplitude of the input pulse train with a settling time of $200\,\text{ns}$ and a residual ripple of approximately $10\,\text{mV}$, that is further filtered by the differential integrator in the AGC network. The simulated statistical mismatch of the two peak detectors voltage offset is $\pm 3.6\,\text{mV}$ (σ), that directly results in an error on the measurement of the amplitude difference between the Signal and Reference. A compensation error of $1\,\%$ requires an amplitude V_{pre} of $360\,\text{mV}$, a value easily managed by the VGA input and the preamplifier output setting a proper gain. The closed-loop bandwidth of the automatic gain control, that directly limits the minimum time per pixel, can be estimated by the linearized loop gain of the system:

$$G_{loop} \approx V_{VGA,ref}^{peak} \frac{dG_{VGA}}{dV_c} \frac{1}{sC_{LPF}R_{LPF}} \qquad (5)$$

where $V_{VGA,ref}^{peak}$ is the peak voltage of the Reference pulse at the output of the VGA and G_{VGA} is the gain of the VGA. The time constant of the differential integrator, $C_{LPF}R_{LPF}$, is set to $250\,\text{ns}$ in order to ensure a stable feedback loop. Given the intrinsic non linearity of the peak detector, the loop gain, and so the settling time of the network, is directly proportional to the amplitude of the incoming signal. By considering a $360\,\text{mV}$ VGA input signal and a $dG_{VGA}/dV_c \approx -0.3\,\text{V}^{-1}$, the time constant is $2.3\,\mu\text{s}$ with a residual compensation error of about 1%. This fast response enables an automatic balancing of the paths suitable for SRS imaging.

D. Analog Subtraction and Demodulation

The common mode fluctuations given by the laser are reduced by the fully differential subtractor shown in Fig. 7a. The subtractor input is AC coupled, in order to filter out the different VGAs output DC voltages. The fully differential architecture shows the same impedance at the input nodes, avoiding an unbalanced amplification of the Reference and Signal path. The ideal differential transfer function is

$$\frac{v_o^{diff}}{v_{in}^{diff}} = \frac{sC_1 R_{eq}}{1 + sC_2 R_{eq}} \qquad (6)$$

with

$$R_{eq} = R_1 \left(1 + \frac{R_3}{R_2}\right) + R_3 \qquad (7)$$

The differential gain is $C_1/C_2 = 16$ between $300\,\text{kHz}$ and $40\,\text{MHz}$ in order to correctly amplify the Raman signal in the full modulation frequency range. By choosing $C_1 = 2\,\text{pF}$ and $C_2 = 125\,\text{fF}$, the required feedback resistance is $4\,\text{M}\Omega$. Such high value resistance is obtained with a T network that increases the value of the physical resistor R_1 by a factor $(1 + R_3/R_2)$. To keep the output DC offset below $\pm 10\,\text{mV}$, we have chosen $R_1 = 800\,\text{k}\Omega$ and $(1 + R_3/R_2) = 5$.
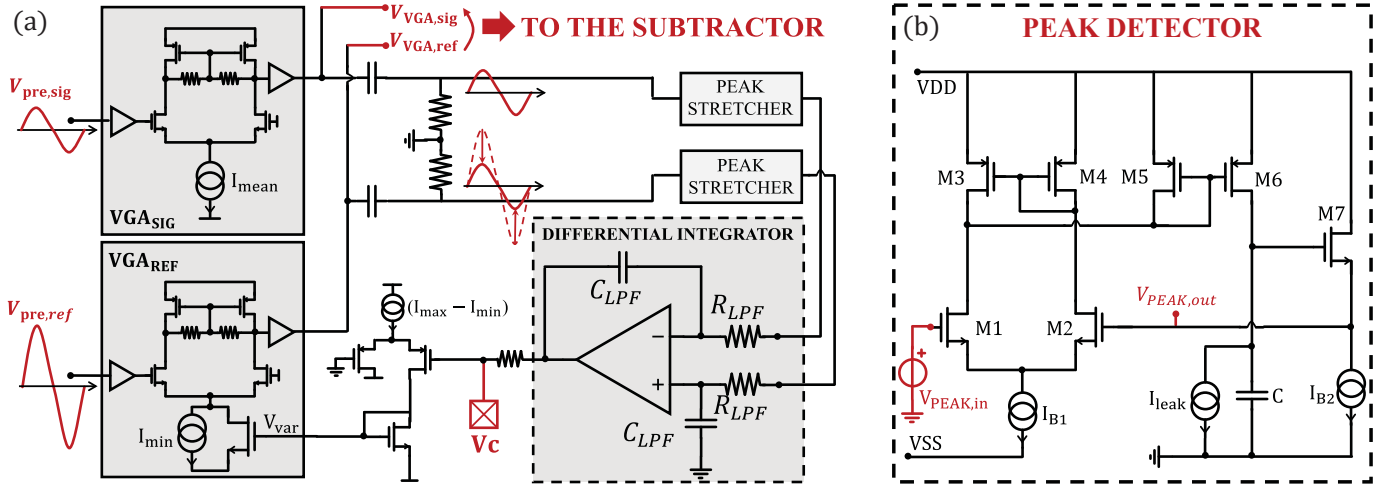
Fig. 6. Block scheme of the Automatic Gain Control network (a) and of the peak discriminator (b).
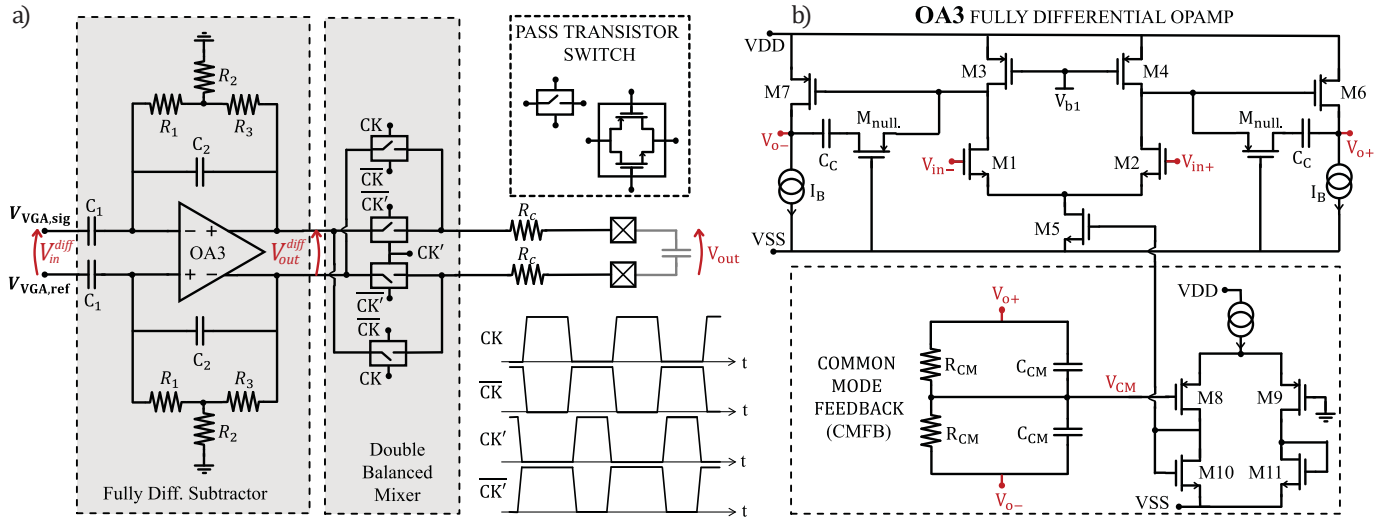

Fig. 7. Architecture of the analog fully differential subtractor and of the mixer (a). Schematic of the fully differential amplifier OA3 (b).

The schematic of the fully differential operational transconductance amplifier (OTA) used for the subtractor is shown in Fig. 7b. It is a standard Miller compensated opamp with a class A output stage. A continuous-time common mode feedback circuit (CMFB) measures the output by means of two high value resistors ($R_{CM} = 800\,\mathrm{k\Omega}$) and regulates the tail current source M5. Two capacitances $C_{CM} = 50\,\mathrm{fF}$ in parallel to R_{CM} enable the CMFB to work up to $40\,\mathrm{MHz}$, enhancing the rejection of the common mode noise at the SRS modulation frequency.

Finally, the SRS signal is demodulated using a passive double-balanced mixer based on four transmission gate switches. The mixer is controlled by four digital signals (in phase, counter-phase and the non overlapped versions) generated on-chip starting from the external clock provided by the optical modulator. The output resistors $R_c = 20\,\mathrm{k\Omega}$ reduce the effect given by the non-linearity of the transmission gates resistances ($150 - 200\,\Omega$) and filter the signal in combination with an off-chip capacitor of $250\,\mathrm{pF}$.

IV. ELECTRICAL CHARACTERISATION

The electronic chip has been implemented in AMS $0.35\,\mathrm{\mu m}$ CMOS technology. The IC die, as shown in Fig. 8, is composed of 4 independent differential channels, uses an area of $4.5\,\mathrm{mm^2}$ and has a nominal power consumption of $\approx 277\,\mathrm{mW}$, when the power supply is $3.3\,\mathrm{V}$. The IC also includes a test channel (not shown in Fig. 8) to simplify the electrical characterisation of each stage.

A. Preamplifier characterisation

Fig. 9 compares the measured preamplifier transfer functions G_{ac} and G_{dc} to the simulated ones, in four gain configurations. The circuit correctly operates as a charge preamplifier in the frequency range of the SRS signal.

Fig. 10 shows the measured input referred current noise spectral density S_{in} of a single channel with the mixer turned off. The noise reaches the minimum in the frequency range of the SRS modulation, 1- $10\,\mathrm{MHz}$, in agreement with Eq. 3. The dotted lines show the shot noise level for the
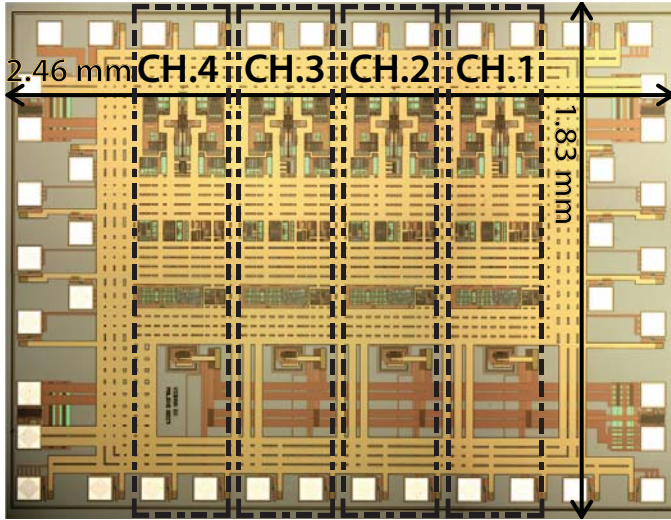
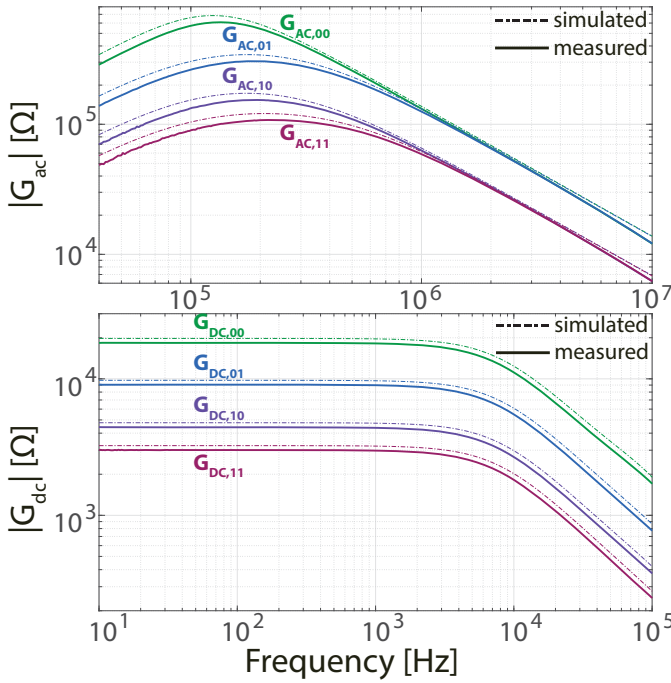Fig. 8. Chip microphotograph with underlined each differential channel.

Fig. 10. Measured and simulated Current input referred noise spectral density of the entire chip in the four possible gain configurations.

Fig. 9. Measured and simulated preamplfier transfer functions of the AC and DC signal path in the four possible gain configurations.

Fig. 11. VGA transfer functions for different control voltage. The bandwidth of the transfer functions is limited at 50 MHz by the measuring setup. The G_{VGA}/V_c function is monotonic (inset).

minimum ($50\,\mu$W) and the maximum ($600\,\mu$W) optical power, confirming an electronic noise lower than the intrinsic limit given by the shot noise in the full optical power range.

B. VGA Characterisation

The VGA transfer function, for different control voltages V_c, is shown in Fig. 11. The measurement is done on the test channel, that has an input and an output pad directly connected to the VGA. The $-3\,$dB bandwidth is $50\,$MHz. It is limited by the capacitive load at the output node added by the experimental setup of about $15\,$pF and the output impedance $R_{out} \cong 200\,\Omega$ of the VGA. The VGAs inside the four channels are expected to have an even broader bandwidth because the
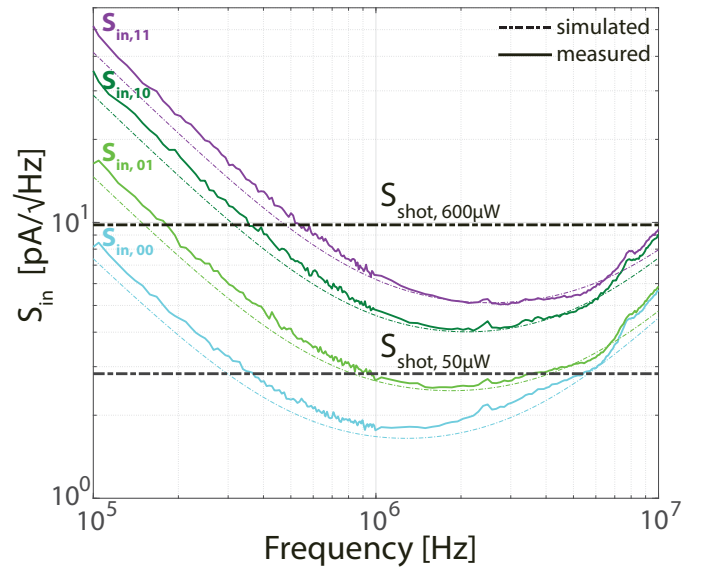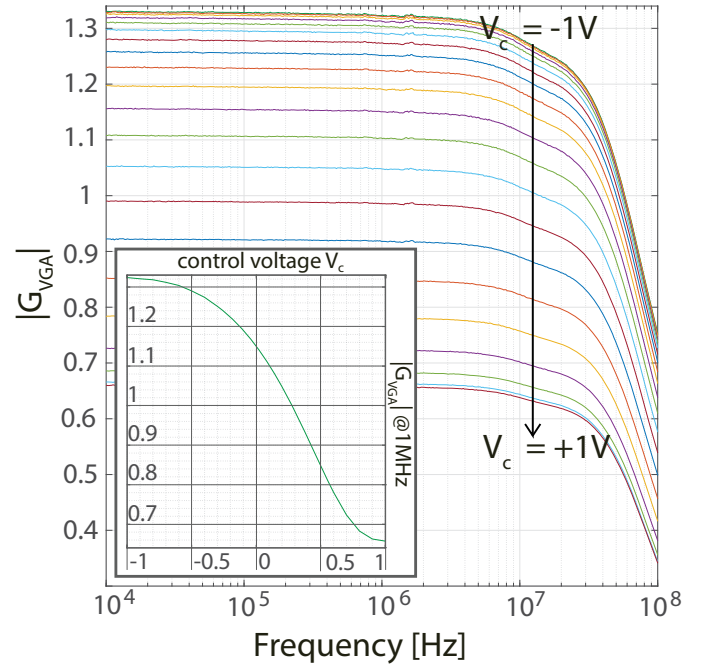
capacitive load is $\approx 2\,$pF given by the subtractor block. The VGA gain at $1\,$MHz as a function of the control voltage V_c is reported in the inset of the Fig. 11. The curve is monotonic, as required for a correct functioning of the AGC network, and shows good linearity in the range $0.95 \pm 30\%$.

C. Autobalancing Network Characterisation

The autobalancing network has been characterized firstly using a fully electrical measurement setup (Fig. 12, top). In order to emulate the excess noise of a laser with repetition rate of $40\,$MHz, we have generated a white voltage noise
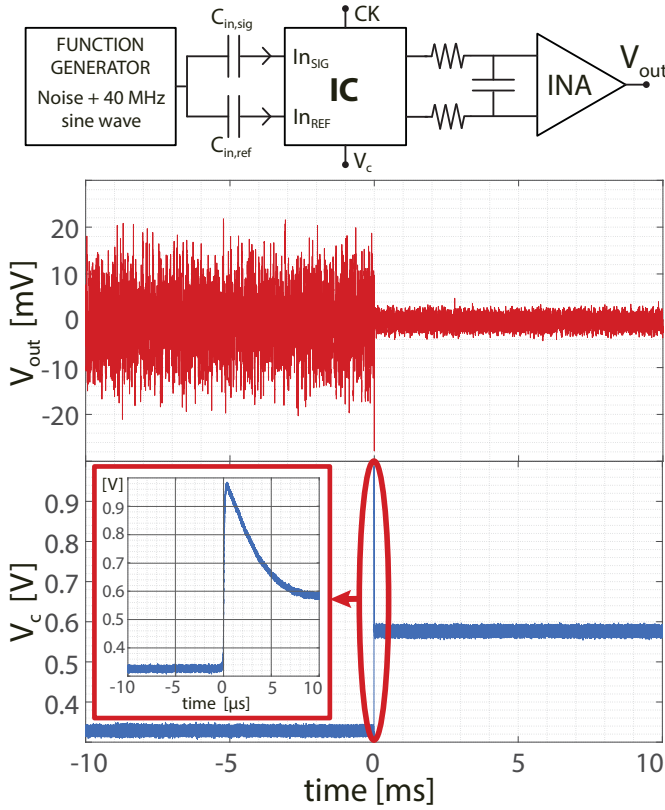
Fig. 12. Output noise and control voltage V_c behavior with the autobalancing network disabled ($t < 0$ s) and enabled ($t > 0$ s). The measurements are done with the simplified experimental setup shown on the top.
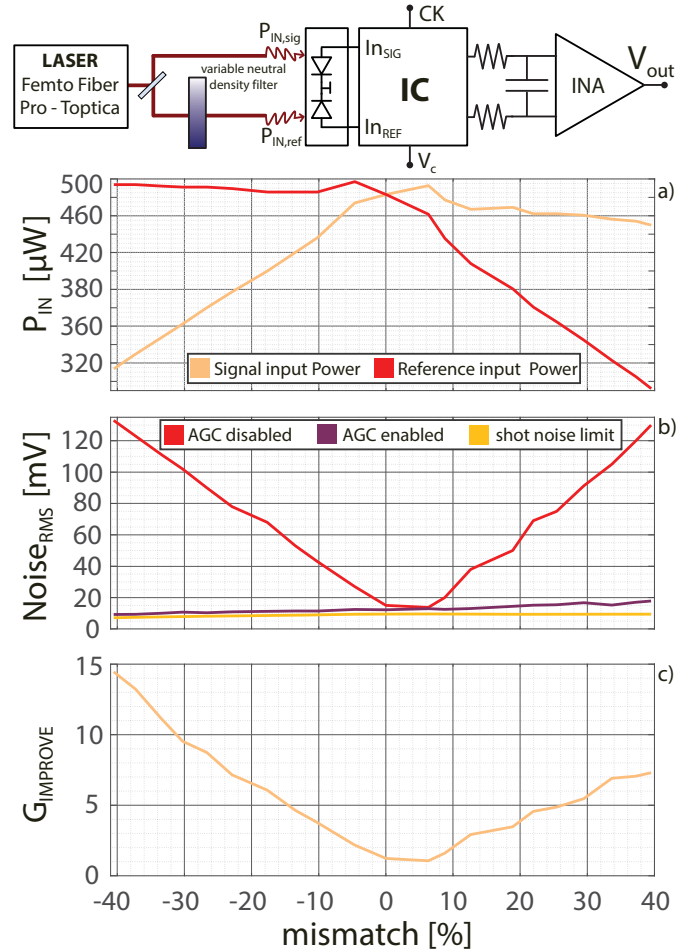

Fig. 13. a) Measured Reference and Signal input optical using the experimental setup shown on the top. The optical power is manually attenuated in order to generate a well controlled power mismatch; b) measured output demodulated noise at 1 MHz as a function of the Reference and Signal mismatches with the Autobalancing network enabled and disabled; c) SNR improving factor $G_{improve}$ given by the autobalancing network.

of $1.0 \frac{\mu V}{\sqrt{Hz}}$ from 0 to $150 \, \text{MHz}$ superimposed to sinusoidal signal at $40 \, \text{MHz}$ with amplitude of $50 \, \text{mV}$. The voltage was converted in two currents and injected in the Reference and Signal preamplifiers virtual ground through two different value capacitors, $C_{in,ref} = 4.7 \, \text{pF}$ and $C_{in,sig} = 3.7 \, \text{pF}$. This results in the generation of two equal in shape and different in amplitude input currents, that are a good approximation of the input signals during a Raman experiment with an optical power of $\approx 100 \, \mu\text{W}$ on the photodiode and a common mode noise ≈ 20 times higher than the shot noise level. The preamplifier was set up with the maximum gain and the control voltage V_c of the VGAs was fixed at $0.375 \, \text{V}$. Reference and Signal channels transfer functions are set with the same gain, while the input signals are mismatched by $23.8 \, \%$ with respect to their mean value. We have applied a $3 \, \text{MHz}$ clock signal to the mixer and we have measured the mixer output voltage with the oscilloscope, after a further amplification of 5 and a low-pass filtering at $6 \, \text{kHz}$, thanks to an external instrumentation amplifier.

Fig. 12 reports the output of the chip with the AGC network disabled (V_c of the Reference path equal to $0.375 \, \text{V}$) and enabled (V_c driven by the internal AGC network). When the control voltage is kept fixed ($t < 0$), the noises injected at the input nodes through the two different value capacitors are unbalanced, reducing the effectiveness of the differential measurement. When the AGC network is enabled ($t > 0$), the feedback loop changes the VGA gain on the Reference path

(Fig. 12, bottom) in order to compensate for the mismatch of the input signals. The output noise is reduced by a factor of 6 and it is limited by the electronic noise of the preamplifier. The settling time of the AGC network (Fig. 12, inset) is $\approx 10 \, \mu\text{s}$ in agreement with Eq. 5.

V. OPTICAL MEASUREMENTS

The autobalancing network was also validated optically (Fig.13), using as laser source the Femto Fiber pro NIR of Toptica Photonics working at $40 \, \text{MHz}$ rate [37]. A pulsed beam with a power of $0.8 \, \text{mW}$ was split in two and focused on the Reference and Signal photodiodes, connected to the first chip channel. The mixer was driven with a $1 \, \text{MHz}$ clock and the output bandwidth limited to $16 \, \text{kHz}$ by an external low pass filter. The relative powers of the beams were manually unbalanced using an optical variable neutral density filter, first on the Signal and then on the Reference beam. The resulting Signal and Reference optical powers are reported in Fig. 13a. The RMS output noise measured with the Autobalancing network enabled and disabled (control voltage

fixed to $V_c = 0.375\,\text{V}$) is reported in Fig. 13b. With the Autobalancing network disabled the noise is fully dominated by the power fluctuations of the laser, in agreement with the initial assumptions. The Autobalancing network restores the symmetry of the acquisition also in case of mismatches of the input powers, strongly reducing the output RMS noise, and bringing it within $3\,\text{dB}$ of the shot noise limit. The SNR is improved up to $23.5\,\text{dB}$ (Fig. 13c), that allows a reduction of the acquisition speed by a factor 225 at a given SNR.

Note that the improvement factor $G_{improve}$ of the SNR is not symmetrical in Fig. 13c. When the Reference power is lower than the Signal power, the AGC increases the VGA gain on the reference path, amplifying the shot noise and the electronic noise. These contributions are not correlated between Signal and Reference channel, thus the total output noise is increased. Therefore, the SNR decreases because the SRS signal is determined by the Signal branch, for which the gain is kept fixed.

A. Multichannel Acquisition of SRS Spectra

The ASIC was mounted in a custom SRS microscope for a full optical validation. The system is similar to the one described in [38]. Briefly, the laser is a mode-locked Yb:fiber laser (Coherent Fidelity) producing 140-fs pulses at 1040 nm with 10 W average power and 80-MHz repetition rate. A 6 W fraction of the laser output is frequency doubled and used to pump an optical parametric oscillator (OPO) that, operating as NSB (Fig. 1), generates the broadband pump pulses with up to 100-mW average power [39] [40]. The spectrum is tunable across the 715-870 nm wavelength range by controlling the cavity length with an amplified piezoelectric actuator. The remaining $4\,\text{W}$ fraction of the laser output is spectrally filtered by an etalon (SLS Optics) to generate narrowband ($\approx 20\,\text{cm}^{-1}$ bandwidth, $1\,\text{ps}$ FWHM duration) Stokes pulses with $1.1\,\text{W}$ average power. The Stokes is modulated at 1-10 MHz by an acousto-optic modulator, which provides up to $75\,\text{mW}$ of a fully modulated beam. Pump and Stokes pulses are temporally synchronized by a mechanical delay line, collinearly combined by a dichroic beam splitter and sent to a home-built transmission microscope, which consists of two confocal plan-achromat long-working-distance objectives with 0.85-NA, 100x magnification and high transmission in the near infrared. Before the beam combiner, a fraction of the pump beam is split to serve as the Reference. After the sample the pump beam, selected by a shortpass filter, is angularly dispersed by a transmission diffraction grating. The dispersed pump spectrum is focused by a lens on the photodiode array.

Fig. 14 reports as points the measured stimulated Raman loss (SRL) spectra of the four different solvents, acetone, methanol, ethanol and acetonitrile, acquired by replacing the microscope objectives with lenses with 25 mm focal length. A prototype board with a single ASIC was mounted on the optical bench and it was moved horizontally in the focal plane of the lens by a mechanical translator, in order to scan sequentially the whole spectrum of the solvent at the output of the diffraction grating. For each position of the detector the SRS signal was recorded. The measurement was then
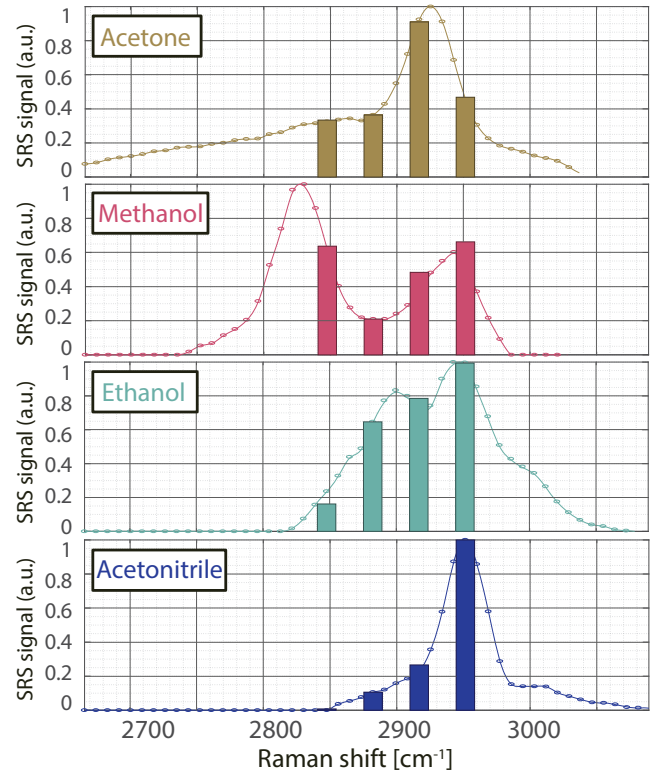

Fig. 14. Points: SRS spectra of different solvents measured with a single ASIC scanned in the focal plane of the lens. Bars: SRS signals measured in parallel with the four-channel detector. The Raman shift is expressed in wavenumber ($\frac{1}{\lambda_p} - \frac{1}{\lambda_s}$). The SRS spectrum is normalized to its maximum.

repeated using the four-channel detector coupled to the four-channel ASIC, kept at a fixed position; the results for the different solvents are reported in Fig. 14 as bar plots. All the SRS spectral profiles agree well with the known spontaneous Raman spectra available in literature [41].

B. Multichannel Image Acquisition of SRS Spectra

The ASIC was also tested for its capability to perform real-time four-channel multiplex SRS microscopy. The microscope is the same used for the solvents spectra acquisition, but the sample is raster scanned in the focal plane of the microscope with a piezo stage.

The SUT chosen for the validation was a mixture of polystyrene (PS) and polymethyl-methacrylate (PMMA) beads, with 3 and 6 μm diameter respectively. The electronic system records the piezo stage position and the four-point SRS spectra in parallel over a 100x100 pixel frame. Fig. 15a shows the measured transmitted mean power for a single frame, where it is not possible to discriminate the beads material. Fig. 15c-f report the SRS images acquired at the four outputs of the chip, each one providing the SRS signal at a different frequency detuning. The images show the capability of the microscope to provide chemical contrast, highlighting the PS beads (panel c) the PMMA beads (panel f) or a response from both beads (panels d and e) according to the selected detection frequency. A chemometric analysis of the image, reported in Fig. 15b, allows to clearly differentiate the two types of beads.
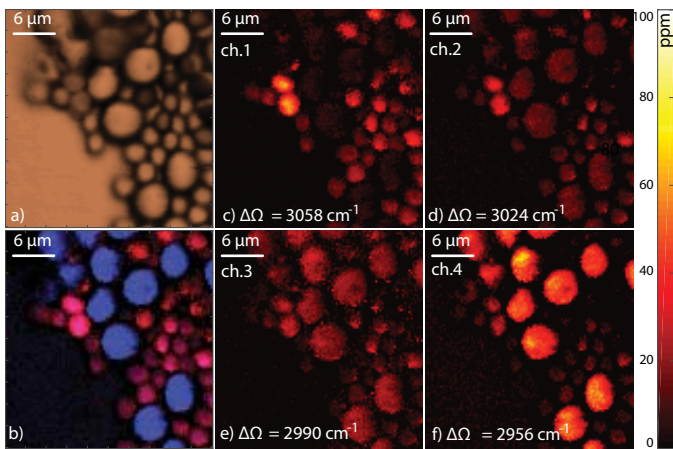
Fig. 15. 100x100 pixel images of a mixture of PS and PMMA beads acquired with a pixel dwell time of $30\,\mu s$ (no averages). The 4 SRS signal frames from ch.1 to ch.4 (c-f) are shown in comparison with the mean input optical power (a). The Raman shift $\Delta\Omega$ is expressed in wavenumber ($\frac{1}{\lambda_p} - \frac{1}{\lambda_s}$). In b) the 4 frames are combined in an RGB image (chemometric analysis).

TABLE I
COMPARISON WITH PREVIOUS WORK

	[22]	[13]	[14]	[21]	[25]	This work
Mod. freq. [MHz]	0.001	0.005	10	2.1	20	$1-10$
P_{SUT} [a] [mW]	84.4	-	24	40	8	62.5
# Channels	128	1 diff.	1 diff.	16	100	4 per IC diff.
AGC t_{sett} [b] [μs]	n.a.	7340	1	n.a	n.a	10
Form factor	comm. instr.	discrete compon.	discrete compon.	discrete compon.	ASIC	ASIC
Resolution[c] [ppm]	2500	56 $6\,\mu W$	SNL[d] $\approx 10\,mW$	SNL[d] $> 200\,\mu W$	≈ 340	SNL[d] $>25\,\mu W$
FoM[e] $\left[\frac{ppm}{\sqrt{Hz}}\right]$	-	0.67	0.70	0.14	-	0.08

[a] Optical power on the sample under test
[b] Settling time of the AGC network, calculated as 3τ of the closed loop bandwidth.
[c] Minimum detectable Raman signal with a time constant of $\tau = 10\,ms$. The optical power on the photodetector is reported when available.
[d] Shot noise limited measurement for a sufficiently high optical power.
[e] A Figure-of-Merit is defined as the estimated minimum detectable Raman signal for an optical power of $100\,\mu W$ normalized to the square root of the bandwidth: $\frac{\Delta I_p}{I_p}|_{100\,\mu W}/\sqrt{BW}$.

The chemical compounds of the beads are well discernible despite a pixel dwell time of only $30\,\mu s$ (3τ), compatible with a near video rate acquisition speed.

Table I summarizes the most relevant specifications of the optical and electronic system discussed in this paper with respect to other experimental setups reported in literature for similar applications. The last row represents the minimum detectable SRS signal normalized to the bandwidth for a fixed input mean power on the photodetector and it can be used as a figure of merit of the electronics readout. The ASIC integrates for the first time in a single chip an autobalanced differential approach with a parallel processing of multiple wavelengths, thus enabling a compact microscope with a fast acquisition limited only by the intrinsic shot noise down to very low power level ($25\,\mu W$).

VI. CONCLUSION

This paper describes a 4-channel ASIC for the parallel readout of the SRS spectrum enabling a fast imaging. The circuit is fabricated, tested and validated in different optical setups and it can be used with flexibility in a wide input power range ($50\,\mu W$ - $600\,\mu W$ per channel). It implements a differential readout to compensate the intensity fluctuations of the laser source and to sensitively extract the SRS signal using the lock-in technique. Each channel includes a gain control circuit to automatically balance the differential architecture for power variations up to $\pm 30\%$, allowing a SNR improvement of $23.5\,dB$ in only $10\,\mu s$ settling time. The ASIC was fully validated by a preliminary 4-channel SRS microscope able to distinguish different chemical compounds with a pixel dwell time of $30\,\mu s$ (3τ). The full multiplex SRS microscope, exploiting 8 chips in parallel for a single shot acquisition of a Raman spectrum with 32 wavelengths, will be presented in an upcoming paper, providing imaging results of biologically relevant samples.

REFERENCES

[1] C. W. Freudiger, W. Min, B. G. Saar, S. Lu, G. R. Holtom, C. He, J. C. Tsai, J. X. Kang, and X. S. Xie, "Label-free biomedical imaging with high sensitivity by stimulated raman scattering microscopy," Science, vol. 322, no. 5909, pp. 1857–1861, 2008.

[2] F. Hu, L. Shi, and W. Min, "Biological imaging of chemical bonds by stimulated raman scattering microscopy," Nature Methods, vol. 16, pp. 830–842, 2019.

[3] J.-X. Cheng and X. S. Xie, "Vibrational spectroscopic imaging of living systems: An emerging platform for biology and medicine," Science, vol. 350, no. 6264, 2015.

[4] D. Fu, "Quantitative chemical imaging with stimulated raman scattering microscopy," Current Opinion in Chemmical Biology, vol. 39, no. 24-31, 2017.

[5] H. Kano, H. Segawa, P. Leproux, and V. Couderc, "Linear and nonlinear raman microspectroscopy: history, instrumentation, and applications," Optical Review, vol. 21, no. 6, pp. 752–761, 2014.

[6] C. Krafft, B. Dietzek, and J. Popp, "Raman and cars microspectroscopy of cells and tissues," Analyst, vol. 134, no. 6, pp. 1046–1057, 2009.

[7] H. Lui, J. Zhao, D. McLean, and H. Zeng, "Real-time raman spectroscopy for in vivo skin cancer diagnosis," Cancer research, vol. 72, no. 10, pp. 2491–2500, 2012.

[8] K. E. Shafer-Peltier, A. S. Haka, M. Fitzmaurice, J. Crowe, J. Myles, R. R. Dasari, and M. S. Feld, "Raman microspectroscopic model of human breast tissue: implications for breast cancer diagnosis in vivo," Journal of Raman Spectroscopy, vol. 33, no. 7, pp. 552–563, 2002.

[9] F. Crisafi, V. Kumar, T. Scopigno, M. Marangoni, G. Cerullo, and D. Polli, "In-line balanced detection stimulated raman scattering microscopy," Scientific reports, vol. 7, no. 1, p. 10745, 2017.

[10] J.-X. Cheng and X. S. Xie, "Vibrational spectroscopic imaging of living systems: An emerging platform for biology and medicine," Science, vol. 350, no. 6264, p. aaa8870, 2015.

[11] D. Zhang, M. N. Slipchenko, and J.-X. Cheng, "Highly sensitive vibrational imaging by femtosecond pulse stimulated raman loss," The journal of physical chemistry letters, vol. 2, no. 11, pp. 1248–1253, 2011.

[12] W. Demtröder, Laser spectroscopy: basic concepts and instrumentation. Springer Science & Business Media, 2013.

[13] K. Seto, Y. Okuda, E. Tokunaga, and T. Kobayashi, "Multiplex stimulated raman imaging with white probe-light from a photonic-crystal fibre and with multi-wavelength balanced detection," Journal of Physics D: Applied Physics, vol. 47, no. 34, 2014.

[14] C. W. Freudiger, W. Yang, G. R. Holtom, N. Peyghambarian, X. S. Xie, and K. Q. Kieu, "Stimulated raman scattering microscopy with a robust fibre laser source," Nature Photonics, vol. 8, no. 2, pp. 153–159, 2014.

[15] D. Polli, V. Kumar, C. M. Valensise, M. Marangoni, and G. Cerullo, "Broadband coherent raman scattering microscopy," Laser & Photonics Reviews, vol. 12, no. 9, 2018.

[16] L. Kong, M. Ji, G. R. Holtom, D. Fu, C. W. Freudiger, and X. S. Xie, "Multicolor stimulated raman scattering microscopy with a rapidly tunable optical parametric oscillator," Optics Letters, vol. 38, no. 2, pp. 145–147, 2013.

[17] Y. Ozeki, W. Umemura, Y. Otsuka, S. Satoh, H. Hashimoto, K. Sumimura, N. Nishizawa, K. Fukui, and K. Itoh, "High-speed molecular spectral imaging of tissue with stimulated raman scattering," Nature Photonics, vol. 6, no. 12, pp. 845–851, 2012.

[18] B. Figueroa, W. Fu, T. Nguyen, K. Shin, B. Manifold, F. Wise, and D. Fu, "Broadband hyperspectral stimulated raman scattering microscopy with a parabolic fiber amplifier source," Biomedical Optics Express, vol. 9, no. 12, 2018.

[19] X. Audier, N. Forget, and H. Rigneault, "Shot noise limited high speed stimulated raman microscopy," arXiv preprint, vol. 1905, no. 11953, 2019.

[20] X. Audier, S. Heuke, P. Volz, I. Rimke, and H. Rigneault, "Noise in stimulated raman scattering measurement: From basics to practice," APL Photonics, vol. 5, no. 1, 2020.

[21] C.-S. Liao, M. N. Slipchenko, P. Wang, J. Li, S.-Y. Lee1, R. A. Oglesbee, and J.-X. Cheng1, "Microsecond scale vibrational spectroscopic imaging by multiplex stimulated raman scattering microscopy," Light: Science & Applications, vol. e265, 2015.

[22] K. Seto, Y. Okuda, E. Tokunaga, and T. Kobayashi, "Development of a multiplex stimulated raman microscope for spectral imaging through multi-channel lock-in detection," Review of Scientific Instruments, vol. 84, no. 8, 2013.

[23] H. Li, Y. Cheng, H. Tang, Y. Bi, Y. Chen, G. Yang, S. Guo, S. Tian, J. Liao, X. Lv, S. Zeng, M. Zhu, C. Xu, J.-X. Cheng, and P. Wang, "Imaging chemical kinetics of radical polymerization with an ultrafast coherent raman microscope," Advanced Science, vol. 7, 2020.

[24] D. X. Lioe, K. Mars, S. Kawahito, K. Yasutomi, K. Kagawa, T. Yamada, and M. Hashimoto, "A stimulated raman scattering cmos pixel using a high-speed charge modulator and lock-in amplifier," Sensors, vol. 16, no. 4, p. 532, 2016.

[25] K. Mars, D. X. Lioe, S. Kawahito, K. Yasutomi, K. Kagawa, T. Yamada, and M. Hashimoto, "Label-free biomedical imaging using high-speed lock-in pixel sensor for stimulated raman scattering," Sensors, vol. 17, no. 281, 2017.

[26] K. Kishore and S. A. Akbar, "Evolution of Lock-In Amplifier as Portable Sensor Interface Platform: A Review," IEEE Sensors Journal, vol. 20, no. 18, pp. 10 345–10 354, sep 2020. [Online]. Available: https://ieeexplore.ieee.org/document/9090194/

[27] A. Ragni, G. Sciortino, M. Sampietro, G. Ferrari, F. Crisafi, V. Kumar, and D. Polli, "Lock-in based differential front-end for raman spectroscopy applications," in 2018 14th Conference on Ph. D. Research in Microelectronics and Electronics (PRIME), 2018, pp. 221–224.

[28] G. Ferrari and M. Sampietro, "Wide bandwidth transimpedance amplifier for extremely high sensitivity continuous measurements," Review of Scientific Instruments, vol. 78, no. 9, p. 094703, 2007.

[29] G. Ferrari, F. Gozzini, A. Molari, and M. Sampietro, "Transimpedance amplifier for high sensitivity current measurements on nanodevices," IEEE J. Solid-State Circuits, vol. 44, no. 5, pp. 1609–1616, 2009.

[30] P. Ciccarella, M. Carminati, G. Ferrari, D. Bianchi, S. Grillanda, F. Morichetti, A. Melloni, and M. Sampietro, "Impedance-sensing cmos chip for non invasive light detection in integrated photonics," IEEE Transactions on Circuits and Systems II: Express Brief, vol. 63, no. 10, pp. 929–933, 2016.

[31] R. Xu, J. Y. Lee, D. Y. Kim, S. Park, Z. Ahmad, and K. O. Kenneth, "0.84-THz imaging pixel with a lock-in amplifier in CMOS," in Digest of Papers - IEEE Radio Frequency Integrated Circuits Symposium, 2016.

[32] V. K. Lazarjan, S. Nazila Hosseini, M. N. Khiarak, and B. Gosselin, "CMOS Optoelectronic Sensor with Ping-pong Auto-zeroed Transimpedance Amplifier," Midwest Symposium on Circuits and Systems, vol. 2020-August, pp. 17–20, 2020.

[33] P. M. Hernandez, M. T. Sanz-Pascual, J. Perez-Bailon, B. Calvo, and N. Medrano, "A CMOS lock-in-based read-out for interdigitated electrodes," I2MTC 2020 - International Instrumentation and Measurement Technology Conference, Proceedings, pp. 3–7, 2020.

[34] P. Ciccarella, M. Carminati, M. Sampietro, and G. Ferrari, "Multichannel 65 zF rms Resolution CMOS Monolithic Capacitive Sensor for Counting Single Micrometer-Sized Airborne Particles on Chip," IEEE Journal of Solid-State Circuits, vol. 51, no. 11, pp. 2545–2553, nov 2016. [Online]. Available: http://ieeexplore.ieee.org/document/7637081/

[35] K. Nose, Y. Ozeki, T. Kishi, K. Sumimura, N. Nishizawa, K. Fukui, Y. Kanematsu, and K. Itoh, "Sensitivity enhancement of fiber-laser-based stimulated raman scattering microscopy by collinear balanced detection technique," optics Express, vol. 20, no. 13, pp. 13 958–13 965, 2012.

[36] S. Caccia and G. Bertuccio, "A 60μW high linearity cmos peak-stretcher/discriminator," IEEE Transactions on Nuclear Science, vol. 54, no. 3, pp. 538–540, 2007.

[37] G. Alessio, V. Kumar, G. Grancini, D. Polli, R. Ramponi, G. Cerullo, and M. Marangoni, "Fiber-format stimulated-raman-scattering microscopy from a single laser oscillator," Optics Letters, vol. 35, no. 2, pp. 226–228, 2010.

[38] A. De la Cadena, C. M. Valensise, M. Marangoni, G. Cerullo, and D. Polli, "Broadband stimulated raman scattering microscopy with wavelength-scanning detection," Journal of Raman Spectroscopy, pp. 1–9, 2020.

[39] N. Coluccelli, D. Viola, V. Kumar, A. Perri, M. Marangoni, G. Cerullo, and D. Polli, "Tunable 30 fs light pulses at 1 w power level from a yb-pumped optical parametric oscillator," Optics letters, vol. 42, no. 21, pp. 4545–4548, 2017.

[40] V. Kumar, A. De la Cadena, A. Perri, F. Preda, N. Coluccelli, G. Cerullo, and D. Polli, "Kumar, vikas, et al. "invited article: Complex vibrational susceptibility by interferometric fourier transform stimulated raman scattering," APL Photonics, vol. 3, no. 9, p. 092403, 2018.

[41] F. Saltarelli, V. Kumar, D. Viola, F. Crisafi, F. Preda, G. Cerullo, and D. Polli, "Broadband stimulated raman scattering spectroscopy by a photonic time stretcher," Optics express, vol. 24, no. 19, pp. 21 264–21 275, 2016.